Electro-Thermal Model for Thermal Disturbance in Cross-Point Phase-Change Memory

Sijung Yoo, Hyung Dong Lee, Seungyun Lee, Hyejung Choi, and Taehoon Kim, *Senior Member, IEEE*

***Abstract*— We developed an electro-thermal model for cross-point phase-change memory (X-PCM) and compared the calculation values with the experimental results. In order to simulate the electro-thermal phenomenon such as thermal disturbance (TDB) of victim cells and reset the current (I_{RESET}) of aggressor cells in a fully confined cross-point structure, a three by three mini-array was constructed with the finite-elemental method. Unlike the conventional thermal model, which only shows the temperature gradient for TDB, our new model can predict the crystallization behavior of victim cells by combining the crystallization model for nucleation and growth. This makes it possible to compare the calculation results with the experimental ones through the crystalline fraction of the victim cell. The simulation results clearly reveal that our new model can closely estimate the victim cell's crystalline fraction for TDB, with the variation of both pulse height (PH) and pulse width (PW) during the RESET operation. Applying the confirmed model for devices of smaller dimensions shows that TDB increases as the device scales down. The increase of TDB is particularly severe as cells become smaller than 16 nm. We suggest that TDB can be reduced not only by decreasing the thermal conductivity (κ) of the interlayer dielectric (ILD), but also by minimizing the PW of the aggressor.**

***Index Terms*— Cross-point memory, electro-thermal modeling, phase-change memory (PCM), reliability, reset current, storage-class memory (SCM), thermal conductivity, thermal disturbance (TDB).**

I. Introduction

PHASE-CHANGE memory (PCM) has been considered as one of the most promising candidates for storage-class memory (SCM) between high-speed dynamic random access memory (DRAM) and high-density NAND Flash, because of its high performance and nonvolatile nature [1]–[4]. However, continuous scaling of DRAM and NAND pushes PCM to be more cost-effective and scalable to satisfy the SCM requirements. Recently, X-PCM has been introduced to satisfy SCM requirements and provide an optimal solution for the modern computing-memory hierarchy [5].

One of the most challenging hurdles when it comes to downscaling PCM is thermal disturbance (TDB), which is an unwanted logic data change of the neighboring cells caused by heat transfer from the cell under reset operation [6]–[8]. The reduction of the distance between cells during downscaling has been thought to be the most critical limit of the PCM. The problem was especially serious in the conventional planar type PCM [7], because the phase-change material (PM) connecting the aggressor and victim cell has relatively high thermal conductivity. On the other hand, X-PCM has a fully confined cell structure with an areal density of $4F^2$, in which PM is surrounded by relatively low thermal conductive insulator. In this structure, the electro-thermal environments of TDB and I_{RESET} will contradict from those of conventional PCM, since TDB and I_{RESET} are determined by the heat balance among heat generation in the aggressor cell, heat transfer to the victim cells, and heat dissipation through other directions.

In this article, we report the development of an electro-thermal model for TDB in X-PCM, and compare the calculated values with the experimental results. Calculation includes theoretical models such as the coupled electro-thermal transport, thermoelectric effect, and the crystallization model which enables us to compare the simulation results with experimental ones. The calculated crystalline fractions by TDB showed a decent match with the experimental results even when we altered the pulse height (PH) and pulse width (PW) for RESET.

Using the confirmed model with physical and material parameters, scaling trends for TDB and I_{RESET} are calculated with different thermal conductivities of interlayer dielectric (ILD) (κ_{ILD}). Since low κ_{ILD} decreases the lateral heat transfer to the victim cells, which can not only reduce TDB, but also reduce I_{RESET} due to the improved thermal confinement effect, and leads to an additional benefit of reduced power consumption [9], [10]. The results show that, as the device scales down, TDB will increase more rapidly and the impact of low κ_{ILD} will become much more important. In order to prevent TDB for devices at 14-nm tech node and below, κ_{ILD} should be mostly around 0.001 W/cm·K. However, the value seems unachievable from typical thermal oxide thin films (κ = 0.006 W/cm·K [11]). Therefore, process-wise, an air gap or thermal boundary layer (TBL) may need to be developed for devices at 14-nm tech node and below. Finally, we discuss another way of reducing TDB in terms of the RESET PW. The result signifies that optimized pulse conditions can reduce the maximum temperature of victim cells to reduce TDB.

II. Electro-Thermal Modeling

In order to simulate the TDB effect, a three by three array of X-PCM cell stack is prepared with finite-element method (FEM). In the real array, each cell stack lies between two

Manuscript received October 3, 2019; revised December 2, 2019; accepted December 9, 2019. Date of publication January 17, 2020; date of current version March 24, 2020. The review of this article was arranged by Editor Y. Shih. *(Corresponding author: Taehoon Kim.)*

The authors are with SK Hynix Inc., Icheon 17336, South Korea (e-mail: taehoon12.kim@sk.com).

Color versions of one or more of the figures in this article are available online at http://ieeexplore.ieee.org.

Digital Object Identifier 10.1109/TED.2019.2960444

0018-9383 © 2020 IEEE. Personal use is permitted, but republication/redistribution requires IEEE permission.
See https://www.ieee.org/publications/rights/index.html for more information.

Authorized licensed use limited to: Intel Corporation via the Virtual Library. Downloaded on October 28,2020 at 21:37:00 UTC from IEEE Xplore. Restrictions apply.

crossing metal lines, i.e., wordline (WL, along y-axis) and bitline (BL, along x-axis), and consists of PM, Ovonic threshold switch (OTS), and electrodes which physically separate the two materials as shown in our previous report [5]. Each cell stack is surrounded by an oxide. Since the experimentally measured data in this article are obtained from the real cell array in our previous report [5], the details of the simulation structure and dimension are also determined to be identical to the real cell, except that a selector layer is removed for the simplicity of simulation. Since the selector is in a highly conductive state during cell operation, its contribution to heat generation is negligible. Instead, an artificial high-resistance layer is inserted to every victim cell in order to prevent the sneak current flow through deselected cells during simulation.

For electro-thermal simulation, the temperature dependence of the resistivity of PM is more important in a confined structure (without heater) than in a planar structure (with heater), since the confined structure is self-heating—meaning it relies on the overall heat generation during heating and melting stages. However, in a planar structure, heating happens more at interfaces and electrodes which is less dependent on the variation of PM resistivity [12]. Thus, the key is how to include the variation of the PM's resistivity during heating and subsequent phase changes [13]. The temperature dependence of resistivity used for simulation is shown in Fig. 1(b). For the efficiency of simulation and convergence of its values, the initial resistivity of PM is set as a constant before beginning of important resistivity changes. The most important region is when the temperature is above 540 K, which is referred from the literature [14], assuming a hexagonal close-packed (HCP) structure, and where the resistivity decreases by the Arrhenius behavior with increasing temperature until melting happens. In addition, the resistivity of molten PM is also set to constant. RESET operations from either crystalline or amorphous phase is assumed to be same, since after the abrupt switch in the amorphous PM, both phases will follow the same dynamic resistance [15]. Thermal conductivity of PM is calculated by the Wiedemann–Franz law as shown in Fig. 1(c)

$$\kappa(T) = LT \cdot \sigma(T) \tag{1}$$

where L is the Lorenz number ($2.44{\cdot}10^{-8}$ W$\cdot\Omega\cdot$K^{-2}).

While the heat generation mechanism in PCM is known as Joule heating, thermoelectric effect also plays a critical role for additional heating and cooling at the hetero-junction, particularly for high-current regions such as the write operation [16]–[18]. As shown in Fig. 1(d), the Seebeck coefficient of PM is determined to be positive with a negative slope before 540 K and a positive slope after 540 K. In addition, its value varies from 122 to 170 μK/V in the temperature range of 300–1000 K [14], [19].

Since TDB is an unwanted crystallization of RESET cells (amorphous phase) happening due to heat transfer from adjacent RESET operations, crystallization kinetics is another important part of the TDB modeling. The Johnson–Mehl–Avrami–Kolmogorov (JMAK) [20]–[22] equation was adopted for simple crystallization modeling, and the JMAK equation can be described as

$$\alpha = 1 - \exp(-(kt)^n) \tag{2}$$

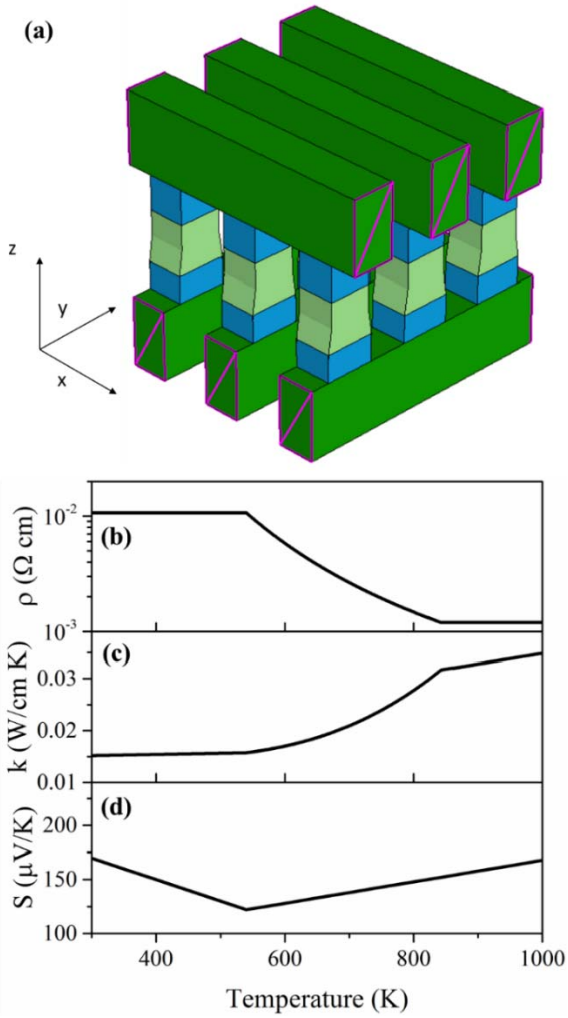

Fig. 1. (a) 3-D view of simulation structure with 3 WLs by 3 BLs cell array. PM (light-green), top and bottom electrode (light-blue) and two orthogonal metal lines (green) are shown. Encapsulating layer, ILD, and artificial resistive layer are deliberately omitted for the clear view of the cell structure. (b)–(d) Electric resistivity, thermal conductivity and Seebeck coefficient of PCM, respectively.

where α is the volume fraction of the transformed phase (crystalline phase in this case), k is the effective rate constant, t is time and n is the Avrami coefficient. In general, k includes both the nucleation and growth rates. Instead of considering the nucleation and growth rate separately, k was determined as a single-modified Arrhenius term in order to simplify the modeling and describe the decay of crystallization rate near melting temperature at the same time [23], which is given by

$$k = k_0 \exp\left(-\frac{E_{a0} + \frac{A}{\Delta G^2}}{k_B T}\right) \tag{3}$$

$$\Delta G = \Delta H_f \cdot \left(1 - \frac{T}{T_m}\right) \tag{4}$$

where k_0 is the frequency factor, E_{a0} is temperature-independent activation energy term, T_m is melting temperature, A is related to interfacial surface free energy between amorphous and crystalline phase, ΔG is the excess Gibbs free energy of the amorphous phase, and ΔH_f is the enthalpy of fusion.

Authorized licensed use limited to: Intel Corporation via the Virtual Library. Downloaded on October 28,2020 at 21:37:00 UTC from IEEE Xplore. Restrictions apply.

The commercially available Sentaurus technology computer-aided design (TCAD) device simulator from Synopsys is used for finite-element modeling. Electric and thermal transport models, as well as the thermoelectric model are implemented by built-in models of the Sentaurus TCAD simulator. Modeling of crystallization was implemented by the physical model interface (PMI) which allows the user to compute user-defined external physical models [24]. Instead of assigning the JMAK equation to the total volume of PCM, it is assigned to each part of the mesh in order to capture the crystallization behavior in the cell, which has a nonuniform distribution of temperature. Computation of crystallization during the application of the electric current pulse follows the procedure below.

1) The JMAK equation is assigned to each finite element (mesh).
2) For each time step $t \sim t + \Delta t$, the temperature distribution, when the current flows, is calculated by coupled electrothermal—thermoelectric models and the temperature of each mesh is determined.
3) Then, the crystallized (transformed) volume fraction of each mesh is calculated by the JMAK equation for the time interval Δt at temperature T.
4) Crystallized fraction of the mesh is updated and then the above steps are repeated for the next time step.

Crystallized volume fraction of the cell after SET operation is measured and simulated for various current pulse conditions as shown in Fig. 2(a). The obtained simulation data set consisting of RESET-PW, −PH, and the crystalline fraction are fit to the measured data by adjusting the parameters of k_0, E_{a0}, A, and n in the JMAK equation to describe the crystallization behavior. The degree of crystallization in the observed cells is calculated from the measured resistance by the effective medium approximation (EMA) [25] assuming a random formation in a spherical crystalline cluster, which is described as

$$\alpha \frac{\sigma_c - \sigma_e}{\sigma_c + 2\sigma_e} + (1-\alpha)\frac{\sigma_a - \sigma_e}{\sigma_a + 2\sigma_e} = 0 \tag{5}$$

where α is the volume fraction of crystal, σ_c, σ_a, and σ_e are the conductivity of crystalline, amorphous phase and measured conductivity, respectively. σ_c, σ_a, and σ_e are obtained from the maximum, minimum, and measured (victim cell) conductivity of the cells, respectively. The maximum and minimum conductivities were measured from the fully crystallized and amorphized PM. The victim cell's conductivity (σ_e) is measured to calculate the crystalline volume fraction (α). In order to calculate the conductivity of PM, the real cell dimension was measured and parasitic resistance terms such as resistance of BL, WL, and top and bottom electrode were excluded using various test patterns.

The time–temperature–transformation (TTT) diagram calculated by the JMAK equation for a single mesh is shown in Fig. 2(b). Since the temperature distribution within the cell is not uniform, each mesh shows different crystallization behavior. This collection of crystallization behaviors in the simulation of SET operation is shown in Fig. 2(d) which is close to the measured result, Fig. 2(c), for the various PWs and PHs, respectively. In spite of a discrepancy in the low-current region, the simulation results of the short-pulse region are in good agreement with the measured crystallization behavior. The overall results indicate that the crystallization modeling with a nonuniform temperature distribution was quite successful. It also confirms that a precise simulation of TDB was executed and agrees with previous reports that the crystallization of victim cells initiates from the side portion of a cell, which is close to the adjacent aggressor cell [8], [26].

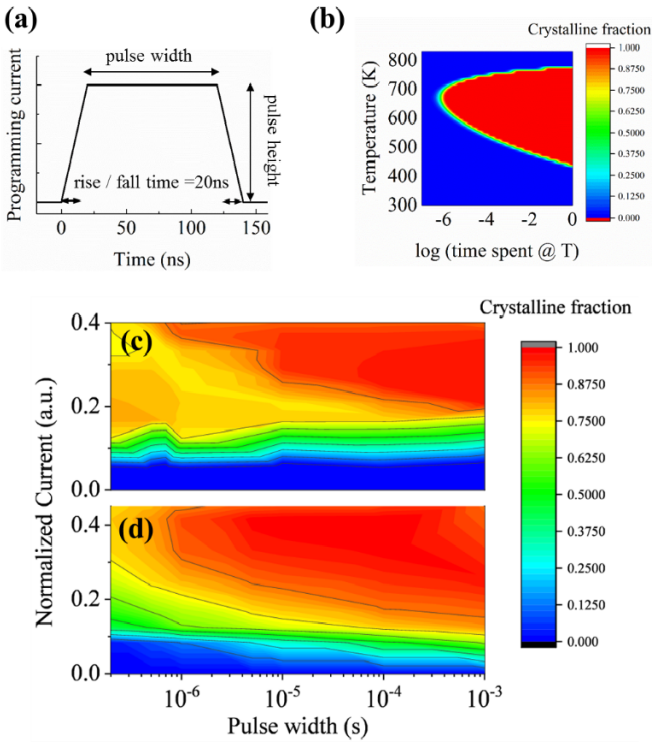

Fig. 2. (a) Electric current pulse shape used in measurement of real cell and simulation input. The pulse has 20 ns of rise and fall time, and the width of the plateau and the height of pulse are varied. Volume fraction of crystalline with respect to the PW and height is measured and simulated to verify and calibrate the simulation parameters. (b) Crystallization behavior depicted by the TTT diagram, which is calculated by JMAK equations with calibrated parameters. The JMAK equation is assigned to every mesh. (c) and (d) are measured and simulated volume fractions of crystalline with respect to various electric pulse conditions.

III. Simulation Results

TDB simulation was implemented and compared with the measurement results to verify the consistency of the simulation as shown in Fig. 3. Since TDB originated from heat generation during RESET operation, if over-RESET happens, TDB will be overestimated. On the other hand, under-RESET may reduce TDB, which will lead to an incomplete RESET. Therefore, we defined the disturbing current (DTC) to indicate the applied current to the aggressor. In the experiment, the amount of TDB was defined by measuring the resistance variation of the victim cell after the application of DTC to the aggressor cell for RESET operation. The measured resistance change is converted to the volume fraction of crystalline PM according to (5). Four different conditions of DTC were applied to

Authorized licensed use limited to: Intel Corporation via the Virtual Library. Downloaded on October 28,2020 at 21:37:00 UTC from IEEE Xplore. Restrictions apply.

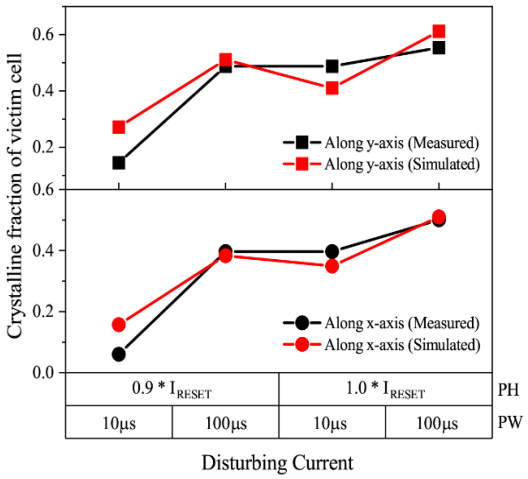

Fig. 3. Simulation results and experimental data of TDB represented by crystalline fraction of adjacent victim cells along the *x*- and *y*-direction. PW and PH of DTC are shown in the *x*-axis. Simulation results are well-matched with the measured experimental data.

the aggressor, and the crystalline volume fraction of the four surrounding victim cells were obtained. The same procedure was applied in simulation, and note that careful consideration was made while setting the physical parameters. Interface resistance (R_{ITF}) between PM and electrodes is set to 1.4 kΩ in order to match with the experimental value of I_{RESET}. Considering that the measured total dynamic resistance of the overall cell stack is 4 kΩ, the value of $R_{\mathrm{ITF}} = 1.4$ kΩ seems reasonable.

In the real cell, I_{RESET} is determined as the minimum current for maximum resistance, while in simulation, I_{RESET} is defined as the minimum current for the temperature of the whole cell to be higher than the T_m. As shown in Fig. 3, crystalline volume fraction of the victim cell, representing the amount of TDB, is quite well matched with the measured value for both x- and y-directions. It is worth noting that the difference of TDB between the x- and y-direction originated from the asymmetric cell to cell space along each direction. Due to the random formation of crystalline inclusions and percolation effect, such changes in crystalline volume fraction will significantly affect the total resistance of a cell [27] and lead to a significant TDB. Particularly, it is worth noting that the results are also in good agreement for different DTCs and PWs. While only a 10% increase in DTC causes the TDB to increase by seven times, an increase in PW by one order is required to cause a similar increase in TDB. The results confirm that the overall simulation model works well and physical parameters are pertinently assigned to match with the real data.

Based on the consistent results, the scaling trend of TDB, represented by crystalline fraction of victim cells along the y-axis, was calculated for different thermal κ_{ILD} in Fig. 4(a). The applied pulse shape of DTC is shown in Fig. 2(a). The PW is set to 1 μs and the PH is determined to be 1.1 times of I_{RESET} to complete RESET. In fact, the 1 μs PW is almost 30–100 times longer than the typical RESET PW which is 10–30 ns, but the effect on TDB is far greater when we consider the heat accumulation during a longer time. The purpose

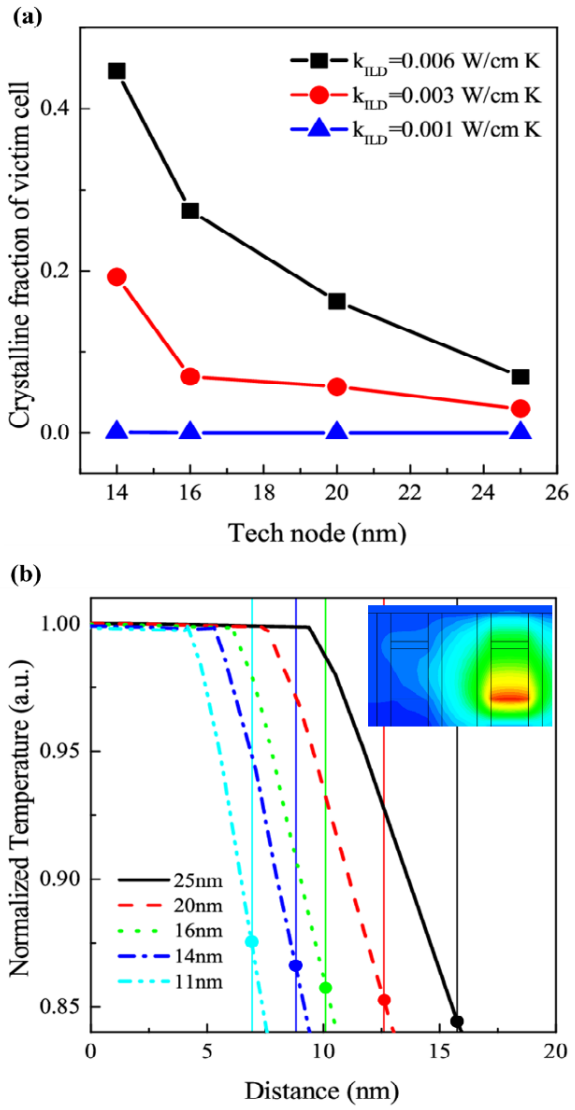

Fig. 4. (a) Simulation results of TDB for each tech node with varying κ_{ILD}. TDB increases as the tech nodes shrink, and the slope of TDB becomes steeper below 16 nm. Using ILD with low κ suppresses TDB significantly. (b) Temperature profile by distance from the center of the aggressor. ILD with $\kappa = 0.003$ W/cm·K is chosen to better show the inflection point of TDB below 16 nm as shown in (a). The vertical lines represent the position of the side wall of the victim cell for each tech node.

of 1 μs pulse is to simplify simulation and to better match the experimental results with the calculated results without unknown parasitic effects of multiple short-pulse conditions. As intuitively expected, TDB becomes worse in the smaller tech node, representing the half pitch of the cell array, since the reduced cell-to-cell distance enhances the lateral heat transfer than in any other directions. Particularly, one can note that the TDB increases more steeply below 16 nm. This is a result of the cell-to-cell distance being so small that the victim cell's temperature rapidly approaches the high-temperature region which is shown in Fig. 4(b), where each data line represents the temperature profile of each tech node from the center of the aggressor cell. Vertical reference lines indicate the location of the nearest sidewall of the victim cell for each tech node, particularly for $\kappa_{\mathrm{ILD}} = 0.003$. It shows the most

Authorized licensed use limited to: Intel Corporation via the Virtual Library. Downloaded on October 28,2020 at 21:37:00 UTC from IEEE Xplore. Restrictions apply.

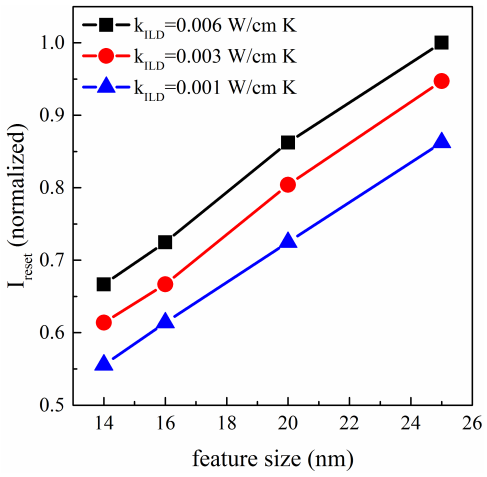

Fig. 5. Simulation result of I_{RESET} for each feature size (tech node). The scaling trend is quite clear due to the Joule heating of reduced dimensions. I_{RESET} is also a function of κ_{ILD}. Right calculation of I_{RESET} should be guaranteed to avoid the miscalculation of TDB.

distinctive slope change below 16 nm. It is clear that each dot, representing the temperature of the sidewall, increases more steeply below 16 nm, which is in good agreement with Fig. 4(a) for $\kappa_{ILD} = 0.003$ W/cm·K.

Since the temperature gradient in X-PCM is determined by the heat balance between lateral heat transfer and vertical heat dissipation, the thermal conductivity of ILD and electrodes will become more important in scaled devices. For example, though increasing vertical heat dissipation may be advantageous to reduce TDB, it is unfavorable in terms of the total power consumption due to the increase of I_{RESET}. On the other hand, blocking lateral heat transfer is expected to bring a net benefit to reduce both TDB and I_{RESET}. As shown in Fig. 4(a), when κ_{ILD} is 0.006 W/cm · K [11], almost 10% of the volume fraction of the victim cell is already crystallized at 25-nm tech node, and over 40% volume is crystallized at 14-nm tech node. When κ_{ILD} is decreased to 0.003 W/cm · K, the crystallized volume fraction of the victim cell reduces to 20% for the 14-nm tech node. Further decrease of κ_{ILD} down to 0.001 W/cm · K may be able to eliminate TDB even at the 14 nm feature size. However, it is scarcely possible to find ILD material with such a low κ_{ILD} and satisfy conformal gap-fill. Therefore, in order to remove TDB below 16 nm, there may need to be a new ILD material and/or the novel integration technology such as controlling porosity or utilizing TBL [28], [29] to satisfy low κ_{ILD}.

Fig. 5 shows the I_{RESET} at each tech node for different κ_{ILD}. Reduction of I_{RESET} from smaller tech nodes, (i.e., smaller feature size) is well understood by the Joule heating theory, in which heat generation is proportional to the current square and resistance ($heat \propto I^2R$). It is worth noting that the evaluation of I_{RESET} is very important for TDB extraction in Fig. 4(a), since applying optimal I_{RESET} for each tech node will guarantee the correct calculation of TDB. Otherwise, an excessive DTC supply larger than $1.1 \times I_{RESET}$ will generate overheating from the aggressor cell, and lead to an overestimation of the TDB for each tech node.

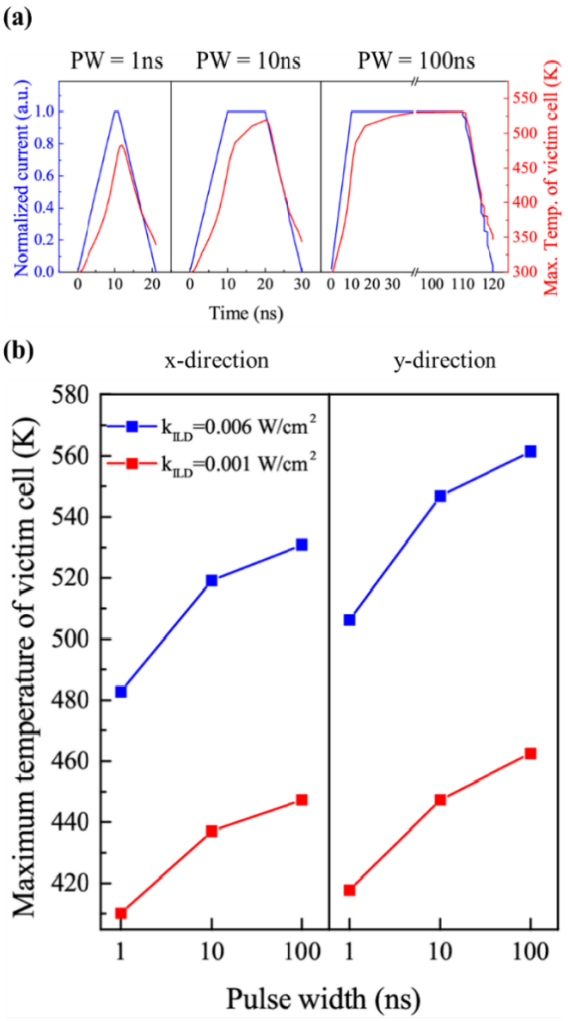

Fig. 6. (a) Electric current pulse applied to the aggressor cell and consequent temperature changes of the victim cell along the *x*-direction in the time domain, for the PW of 1, 10, 100 ns. In order for the victim cell to reach the maximum temperature, there exists a time delay, called thermal latency. (b) Maximum temperature of the victim cell along the *x*- and *y*-directions with respect to PW applied to the aggressor cell. The result shows that the combined effect of short PW with low κ_{ILD} can reduce TDB significantly.

Another possible way to reduce TDB is to shorten the PW of DTC, i.e., apply the aggressor's RESET PW as short as possible, unless the RESET characteristics degrade. As already emphasized in Fig. 3, the PW of DTC can be critical for TDB and particularly more sensitive when the PH of DTC is small. This is because while PH only affects heat generation, PW affects both heat generation and transfer. For that reason, when DTC is small, TDB will be more sensitive to PW, however, when DTC is sufficient TDB will be less sensitive to PW.

Furthermore, there is an additional benefit of short PW below a few tens of nanoseconds. As shown in Fig. 6(a), there is a "time delay" effect, known as thermal latency, from the heat generation of the aggressors to the temperature rise of the victim cell. Although the current pulse reached its plateau region at the aggressor, the temperature of the victim cell was not saturated yet. An additional 30 ns is required for the victim cell to reach the saturation temperature. In other words,

Authorized licensed use limited to: Intel Corporation via the Virtual Library. Downloaded on October 28,2020 at 21:37:00 UTC from IEEE Xplore. Restrictions apply.

if RESET PW can be made shorter than 30 ns, the total amount of heat experienced by the victim cell can be decreased. In Fig. 6(b) the effect of PW on the maximum temperature of the victim cell is plotted. The maximum temperature of the victim cell can be decreased by more than 50 K by decreasing t_{RESET} to 1 ns for both the x- and y-directions. The effect of κ_{ILD} can be considered to be the same way. Therefore, the combined effect of short PW of RESET and low κ_{ILD} can lower the maximum temperature of victim cells down by 70–100 K, which is a huge benefit for decreasing TDB.

IV. Conclusion

We have presented a new electro-thermal model for TDB in PCM-based X-point memory and compared the calculation results with the experimental ones. The model includes coupled electric and thermal transport, thermoelectric effect, and crystallization model.

The calculated results match well with the experimental ones even when changing with PH and PW of DTC. Based on the confirmed simulation model, the scaling trend of TDB was also predicted. As expected, TDB increases as tech nodes get smaller, especially below 16 nm, where the increase in rate becomes faster. Application of low κ_{ILD} can significantly reduce the TDB, but to completely get rid of TDB below 16-nm tech node, we must either use a new ILD material or lower κ_{ILD} by applying TBL or forming airgap. Application of short RESET PW will be another way to reduce TDB, and controller technology may also be helpful to satisfy the product specification for TDB by limiting the maximum number of RESET operations.

In conclusion, we think that our new model can provide useful insight for the materials development, process integration, and design of operation algorithms to continue the scaling of PCM in the future.

References

[1] H.-S. P. Wong *et al.*, "Phase change memory," *Proc. IEEE*, vol. 98, no. 12, pp. 2201–2227, Dec. 2010, doi: 10.1109/JPROC.2010.2070050.

[2] G. W. Burr *et al.*, "Recent progress in phase-change memory technology," *IEEE Trans. Emerg. Sel. Topics Circuits Syst.*, vol. 6, no. 2, pp. 146–162, Jun. 2016, doi: 10.1109/JETCAS.2016.2547718.

[3] S. Lai, "Current status of the phase change memory and its future," in *IEDM Tech. Dig.*, Dec. 2003, pp. 255–258, doi: 10.1109/IEDM.2003.1269271.

[4] S. W. Fong, C. M. Neumann, and H.-S. P. Wong, "Phase-change memory—Towards a storage-class memory," *IEEE Trans. Electron Devices*, vol. 64, no. 11, pp. 4374–4385, Nov. 2017, doi: 10.1109/TED.2017.2746342.

[5] T. Kim *et al.*, "High-performance, cost-effective 2z nm two-deck cross-point memory integrated by self-align scheme for 128 Gb SCM," in *IEDM Tech. Dig.*, Dec. 2018, pp. 37.1.1–37.1.4, doi: 10.1109/IEDM.2018.8614680.

[6] A. Privano, A. L. Lacaita, A. Benvenuti, F. Pellizzer, S. Hudgens, and R. Bez, "Scaling analysis of phase-change memory technology," in *IEDM Tech. Dig.*, Dec. 2003, pp. 699–702, doi: 10.1109/IEDM.2003.1269376.

[7] U. Rosso, D. Ielmini, A. Redaelli, and A. L. Lacaita, "Modeling of programming and read performance in phase-change memories—Part II: Program disturb and mixed-scaling approach," *IEEE Trans. Electron Devices*, vol. 55, no. 2, pp. 515–522, Feb. 2008, doi: 10.1109/TED.2007.913573.

[8] S. Kim *et al.*, "Thermal disturbance and its impact on reliability of phase-change memory studied by the micro-thermal stage," in *Proc. IEEE Int. Rel. Phys. Sym.*, May 2010, pp. 99–103, doi: 10.1109/IRPS.2010.5488847.

[9] E. Bozorg-Grayeh, J. P. Reifenberg, M. Asheghi, H.-S. P. Wong, and K. E. Goodson, "Thermal transport in phase change memory materials," *Annu. Rev. Heat Transf.*, vol. 16, no. 13, pp. 397–428, 2013, doi: 10.1615/AnnualRevHeatTransfer.v16.130.

[10] S. B. Kim and H.-S. P. Wong, "Analysis of temperature in phase change memory scaling," *IEEE Electron Devices Lett.*, vol. 28, no. 8, pp. 697–699, Aug. 2007, doi: 10.1109/LED.2007.901347.

[11] T. Yamane, N. Nagai, S. Katayama, and M. Todoki, "Measurement of thermal conductivity of silicon dioxide thin films using a 3ω method," *J. Appl. Phys.*, vol. 91, pp. 9772–9776, 2002, doi: 10.1063/1.1481958.

[12] D. H. Im *et al.*, "A unified 7.5 nm dash-type confined cell for high performance PRAM device," in *IEDM Tech. Dig.*, Dec. 2008, pp. 1–4, doi: 10.1109/IEDM.2008.4796654.

[13] T. Kato and K. Tanaka, "Electronic properties of amorphous and crystalline $Ge_2Sb_2Te_5$ films," *Jpn. J. Appl. Phys.*, vol. 44, no. 10, pp. 7340–7344, Oct. 2005, doi: 10.1143/JJAP.44.7340.

[14] L. Adnane *et al.*, "High temperature electrical resistivity and Seebeck coefficient of $Ge_2Sb_2Te_5$ thin films," *J. Appl. Phys.*, vol. 122, Sep. 2017, Art. no. 125104, doi: 10.1063/1.4996218.

[15] A. Pirovano, A. L. Lacaita, A. Benvenuti, F. Pellizzer, and R. Bez, "Electronic switching in phase-change memories," *IEEE Trans. Electron Devices*, vol. 55, no. 3, pp. 452–459, Mar. 2004, doi: 10.1109/TED.2003.823243.

[16] J. Bahl, B. Rajendran, and B. Muralidharan, "Programming current reduction via enhanced asymmetry-induced thermoelectric effects in vertical nanopillar phase-change memory cells," *IEEE Trans. Electron. Devices*, vol. 62, no. 12, pp. 4015–4021, Dec. 2015, doi: 10.1109/TED.2015.2486142.

[17] A. Faraclas *et al.*, "Modeling of thermoelectric effects in phase change memory cells," *IEEE Trans. Electron. Devices*, vol. 61, no. 2, pp. 372–378, Feb. 2014, doi: 10.1109/TED.2013.2296305.

[18] J. Lee, M. Asheghi, and K. Goodson, "Impact of thermoelectric phenomena on phase-change memory performance metrics and scaling," *Nanotechnology*, vol. 23, no. 20, Apr. 2012, Art. no. 205201, doi: 10.1088/0957-4484/23/20/205201.

[19] J. Lee, T. Kodama, Y. Won, M. Asheghi, and K. Goodson, "Phase purity and the thermoelectric properties of $Ge_2Sb_2Te_5$ films down to 25 nm thickness," *J. Appl. Phys.*, vol. 112, Jul. 2012, Art. no. 014902, doi: 10.1063/1.4731252.

[20] M. Avrami, "Kinetics of phase change. I. General theory," *J. Chem. Phys.*, vol. 7, no. 12, pp. 1103–1112, Dec. 1939, doi: 10.1063/1.1750380.

[21] M. Avrami, "Kinetics of phase change. II. Transformation-time relations for random distribution of nuclei," *J. Chem. Phys.*, vol. 8, no. 2, pp. 212–224, Feb. 1940, doi: 10.1063/1.1750631.

[22] M. Avrami, "Kinetics of phase change. III. Granulation, phase change, and microstructure," *J. Chem. Phys.*, vol. 9, no. 177, 1941, doi: 10.1063/1.1750872.

[23] C. Peng, L. Cheng, and M. Mansuripur, "Experimental and theoretical investigations of laser-induced crystallization and amorphization in phase-change optical recording media," *J. Appl. Phys.*, vol. 82, pp. 4183–4191, Aug. 1997, doi: 10.1063/1.366220.

[24] *Sentaurus Device User Guide*, Synopsys, Mountain View, CA, USA, 2008.

[25] R. Landauer, "Electrical conductivity in inhomogeneous media," in *Proc. AIP Conf.*, Apr. 1978, vol. 40, no. 2, pp. 2–45, doi: 10.1063/1.31150.

[26] A. Redaelli *et al.*, "Interface engineering for thermal disturb immune phase change memory technology," in *IEDM Tech. Dig.*, Dec. 2013, pp. 30.4.1–30.4.4, doi: 10.1109/IEDM.2013.6724724.

[27] D. H. Kim, F. Merget, M. Laurenzis, P. H. Bolivar, and H. Kurz, "Electrical percolation characteristics of $Ge_2Sb_2Te_5$ and Sn doped $Ge_2Sb_2Te_5$ thin films during the amorphous to crystalline phase transition," *J. Appl. Phys.*, vol. 97, Apr. 005, Art. no. 083538, doi: 10.1063/1.1875742.

[28] S. W. Fong, C. M. Neumann, and H.-S. P. Wong, "Dual-layer dielectric stack for thermally-isolated low-power phase-change memory," in *Proc. IEEE Int. Memory Workshop*, May. 2017, pp. 1–4, doi: 10.1109/IMW.2017.7939079.

[29] J. P. Reifenberg, D. L. Kencke, and K. E. Goodson, "The impact of thermal boundary resistance in phase-change memory devices," *IEEE Electron Devices Lett.*, vol. 29, no. 10, pp. 1112–1114, Oct. 2008, doi: 10.1109/LED.2008.2003012.

Authorized licensed use limited to: Intel Corporation via the Virtual Library. Downloaded on October 28,2020 at 21:37:00 UTC from IEEE Xplore. Restrictions apply.